



Modifier cation effects on ^{29}Si nuclear shielding anisotropies in silicate glasses



Jay H. Baltisberger^a, Pierre Florian^b, Eric G. Keeler^d, Pyae A. Phy^a, Kevin J. Sanders^e, Philip J. Grandinetti^{c,*}

^a Division of Natural Science, Mathematics, and Nursing, Berea College, Berea, KY 40403, United States

^b CNRS, UPR3079 CEMHTI, 1D Avenue de la Recherche Scientifique, 45071 Orléans Cedex 2, France

^c Department of Chemistry, The Ohio State University, 120 W. 18th Avenue, Columbus, OH 43210-1173, United States

^d Department of Chemistry and Francis Bitter Magnet Laboratory, Massachusetts Institute of Technology, 77 Massachusetts Avenue, Cambridge, MA 02139, United States

^e Institut des Sciences Analytiques (CNRS, ENS de Lyon, UCB Lyon 1), Université de Lyon, 5 rue de la Doua, 69100 Villeurbanne, France

ARTICLE INFO

Article history:

Received 20 August 2015

Revised 29 April 2016

Accepted 8 May 2016

Available online 9 May 2016

Keywords:

^{29}Si NMR

Magic-angle flipping

Nuclear shielding tensor

Alkali silicate glass

Alkaline earth silicate glass

Silicate disproportionation

Paramagnetic relaxation enhancement

Echo train acquisition

ABSTRACT

We have examined variations in the ^{29}Si nuclear shielding tensor parameters of SiO_4 tetrahedra in a series of seven alkali and alkaline earth silicate glass compositions, $\text{Cs}_2\text{O} \cdot 4.81 \text{ SiO}_2$, $\text{Rb}_2\text{O} \cdot 3.96 \text{ SiO}_2$, $\text{Rb}_2\text{O} \cdot 2.25 \text{ SiO}_2$, $\text{K}_2\text{O} \cdot 4.48 \text{ SiO}_2$, $\text{Na}_2\text{O} \cdot 4.74 \text{ SiO}_2$, $\text{BaO} \cdot 2.64 \text{ SiO}_2$, and $\text{SrO} \cdot 2.36 \text{ SiO}_2$, using natural abundance ^{29}Si two-dimensional magic-angle flipping (MAF) experiments. Our analyses of these 2D spectra reveal a linear dependence of the ^{29}Si nuclear shielding anisotropy of $Q^{(3)}$ sites on the Si–non-bridging oxygen bond length, which in turn depends on the cation potential and coordination of modifier cations to the non-bridging oxygen. We also demonstrate how a combination of Cu^{2+} as a paramagnetic dopant combined with echo train acquisition can reduce the total experiment time of ^{29}Si 2D NMR measurements by two orders of magnitude, enabling higher throughput 2D NMR studies of glass structure.

© 2016 Elsevier Inc. All rights reserved.

1. Introduction

Silicate glass structure is often modeled as a continuous random network of interconnected silicate tetrahedra [1,2]. Within this model are five types of silicate tetrahedra each classified by their connectivity, i.e., the number of oxygen that are corner-linked to other tetrahedra. These are denoted by the notation $Q^{(n)}$, where n ($=0$ –4) represents the number of bridging oxygen per tetrahedron. Quantifying the distribution of $Q^{(n)}$ species in a silicate glass and their degrees of connectivity can provide considerable insight into the structure of glass [3,4] as well as into the reactions of anionic species occurring in the melt [4–11].

NMR has played and continues to play a significant role in identifying and validating glass structural models [3,12,13]. For example, regarding short-range order in silicate glasses, 1D ^{29}Si MAS spectra [12,14–20] has provided convincing evidence that the $Q^{(n)}$

species distribution is not random but closer to binary, that is, the glass contains a maximum of two $Q^{(n)}$ species, with a sequential appearance of $Q^{(n-1)}$ species as the alkali content increases. Related to these efforts Stebbins [21] showed that the characteristically different anisotropic lineshapes of $Q^{(n)}$ sites can be exploited in a static sample (non-MAS) ^{29}Si NMR measurements to observe and quantify the narrow resonances of $Q^{(4)}$ at lower abundance. With the introduction of 2D isotropic/anisotropic correlation experiments, like ^{29}Si 2D magic-angle flipping (MAF) [6,7,10,11], the precision for quantifying all $Q^{(n)}$ sites was dramatically improved, allowing $Q^{(n)}$ species to be identified and quantified even when the 1D MAS spectrum is completely unresolved [7,11].

An approximate approach for understanding the systematic variation in the ^{29}Si nuclear shielding tensors of $Q^{(n)}$ sites can be found through straightforward symmetry arguments. As a traceless second-rank symmetric tensor the shielding anisotropy tensor vanishes for the central atom in a tetrahedral bonding arrangement. This is the case in both fully connected $Q^{(4)}$ and fully disconnected $Q^{(0)}$ sites where the four Si–O bond have approximately equal lengths. In $Q^{(1)}$, $Q^{(2)}$, and $Q^{(3)}$ sites, however, there are signif-

* Corresponding author.

E-mail address: grandinetti.1@osu.edu (P.J. Grandinetti).

icant differences among the four bond lengths with silicon–non-bridging oxygen (Si–NBO) bonds typically a few picometers shorter than silicon–bridging oxygen (Si–BO) bonds. As noted by Grimmer and coworkers [22,23] as the bond length decreases there will be an increase in s character of the bonding orbital and an increased shielding along the direction of the shorter bond. Thus, the ^{29}Si shielding tensor of $Q^{(3)}$ is axially symmetric with the largest shielding component along the shorter Si–NBO bond. Similar arguments explain the axially symmetric shielding tensor of $Q^{(1)}$ sites with the smallest shielding component along longer Si–BO bond. For $Q^{(2)}$ the shielding tensor is non-axially symmetric with largest shielding component along the axis that bisects the NBO–Si–NBO angle.

As the number of ^{29}Si 2D MAF measurements [24,25] in alkali and alkaline earth silicate glasses [6,7,10,11] increased, we noted a systematic decrease in the ^{29}Si nuclear shielding anisotropy for $Q^{(n)}$ sites with increasing modifier cation potential [11]. This was explained by an increase in Si–NBO bond lengths when coordinated by stronger modifier cations. That is, as the Si–NBO bond gets closer in length to the Si–BO length a reduced ^{29}Si shielding anisotropy is observed. Similar systematic cation effects on isotropic and anisotropic chemical shifts were observed in phosphate glasses by Kirkpatrick and coworkers [26,27]. If this linear dependence could be experimentally calibrated in silicate glasses the ^{29}Si nuclear shielding anisotropy would become a more powerful probe of microscopic structure in glasses.

In this paper we examine the variation in ^{29}Si nuclear shielding anisotropy of $Q^{(3)}$ sites of seven different alkali and alkaline-earth glass compositions using ^{29}Si 2D MAF NMR. To enable these measurements at natural abundance ^{29}Si levels we combine echo train acquisition with paramagnetic Cu^{2+} dopant in the glass [28,29,16,17,30,31] as it dramatically reduces the ^{29}Si T_1 values, i.e., recycle delays, without significant reductions in T_2 . Our analyses of these 2D spectra reveal the dependence of the ^{29}Si nuclear shielding anisotropy of $Q^{(3)}$ sites on the changing network modifier cation potential, and also suggest a related dependence on the changing coordination of modifier cations to the non-bridging oxygen. These results not only help us better understand ^{29}Si nuclear shielding tensor anisotropies but also impact our efforts in discovering new structures and structural trends in silicate glasses.

2. Methods

2.1. Sample preparation

Alkali and alkaline earth oxide silicate glasses with nominal compositions given in Table 1 were synthesized from high-purity metal carbonates (Aldrich 99+%) and silica (Aldrich 99.99% metals basis). Approximately 0.5 wt% of CuO was added to each composition to shorten the spin–lattice relaxation time, T_1 . An additional barium silicate glass was prepared without addition of CuO for comparison purposes. Prior to synthesis, metal carbonates and silica were placed in a dehydrating oven at 150°C overnight to remove any water from the materials. The starting materials were ground to get homogeneous mixtures, decarbonated at 700°C (and 600°C for glasses made with K_2O) overnight and then melted for about 2 h at the temperatures given in Table 1. The samples were then quenched from these temperatures to room temperature by placing the bottom of the platinum crucible into water. The recovered samples were fully transparent and possessed a very uniform light blue color, indicating the copper is uniformly distributed.

Due to the hygroscopic nature of the metal carbonates used in the syntheses as well as the low melting points and high volatility of alkali metal oxides [32,33] the integrated areas of $Q^{(n)}$ resonances obtained from the ^{29}Si MAF spectrum (vide infra) were used to determine the final stoichiometric ratio of alkali metal oxide to

Table 1

Nominal sample compositions, melt temperatures, and NMR corrected compositions of alkali and alkaline silicate glasses used in this study. For composition $\text{M}_{2/2}\text{O} \cdot w\text{SiO}_2$ we have $w = n_{\text{Si}}/(zn_M/2)$. All compositions are doped with approximately 0.5 wt% CuO except $\text{BaO} \cdot 2.75 \text{SiO}_2$.

Nominal composition	Melt temp. ($^\circ\text{C}$)	Corrected composition
$\text{Cs}_2\text{O} \cdot 4.5 \text{SiO}_2$	1300	4.81 ± 0.05
$\text{Rb}_2\text{O} \cdot 4.0 \text{SiO}_2$	1300	3.96 ± 0.02
$\text{Rb}_2\text{O} \cdot 2.0 \text{SiO}_2$	1200	2.25 ± 0.003
$\text{K}_2\text{O} \cdot 4.0 \text{SiO}_2$	1100	4.48 ± 0.01
$\text{Na}_2\text{O} \cdot 4.0 \text{SiO}_2$	1300	4.74 ± 0.02
$\text{BaO} \cdot 2.0 \text{SiO}_2$	1500	2.64 ± 0.03
$\text{BaO} \cdot 2.0 \text{SiO}_2$	1500	2.75 ± 0.02
$\text{SrO} \cdot 2.0 \text{SiO}_2$	1500	2.36 ± 0.53

silica in the final composition, $\text{M}_{2/2}\text{O} \cdot w\text{SiO}_2$. Combining the stoichiometric ratio

$$w = \frac{2}{z} \frac{n_{\text{Si}}}{n_M}, \quad (1)$$

with the charge balance equation

$$zn_M = 4n_{Q^0} + 3n_{Q^1} + 2n_{Q^2} + n_{Q^3}, \quad (2)$$

where n_M and n_{Q^n} are the number of moles of metal oxide and $Q^{(n)}$ species, respectively, one obtains the expression

$$w = \frac{2}{4y_{Q^0} + 3y_{Q^1} + 2y_{Q^2} + y_{Q^3}}, \quad (3)$$

where y_i are the mole fractions taken as the integrated areas of the $Q^{(n)}$ resonances given in Table 5. The adjusted compositions are

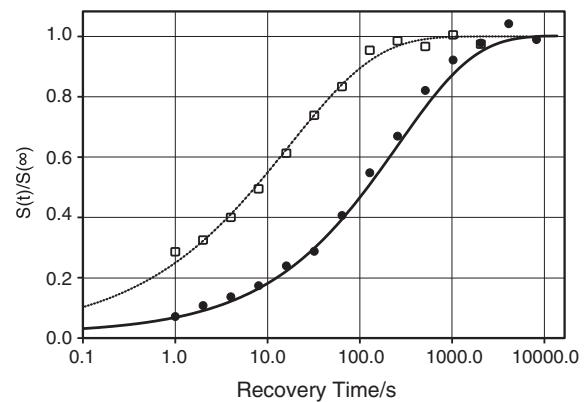


Fig. 1. The ^{29}Si magnetization saturation recovery on a logarithmic time axis for undoped (solid circles) and 0.5 wt% CuO -doped (open squares) barium silicate glass along with best-fit to the stretched exponential function of Eq. (4).

Table 2

Best fit parameters from least-squares analysis of saturation recovery experiments to the stretched exponential function of Eq. (4). Parameter uncertainties are given as one standard deviation. Also listed for each composition is the chi-squared reduced, χ_v^2 , for the best fit and $T_{75\%}$, the 75% recovery time. All compositions are doped with approximately 0.5 wt% CuO except $\text{BaO} \cdot 2.75 \text{SiO}_2$.

Composition	T_1 (s)	β	χ_v^2	$T_{75\%}$ (s)
$\text{Cs}_2\text{O} \cdot 4.81 \text{SiO}_2$	3.65 ± 0.1	0.48 ± 0.01	1.5	7.2
$\text{Rb}_2\text{O} \cdot 3.96 \text{SiO}_2$	2.16 ± 0.15	0.37 ± 0.02	1.4	5.7
$\text{Rb}_2\text{O} \cdot 2.25 \text{SiO}_2$	1.76 ± 0.09	0.54 ± 0.02	1.5	3.2
$\text{K}_2\text{O} \cdot 4.48 \text{SiO}_2$	4.02 ± 0.20	0.43 ± 0.03	1.8	8.5
$\text{Na}_2\text{O} \cdot 4.74 \text{SiO}_2$	7.32 ± 0.40	0.53 ± 0.02	1.4	13.5
$\text{BaO} \cdot 2.64 \text{SiO}_2$	16.4 ± 0.7	0.48 ± 0.02	1.6	33
$\text{BaO} \cdot 2.75 \text{SiO}_2$	226 ± 6	0.52 ± 0.02	1.9	423
$\text{SrO} \cdot 2.36 \text{SiO}_2$	39 ± 2	0.49 ± 0.02	1.6	75

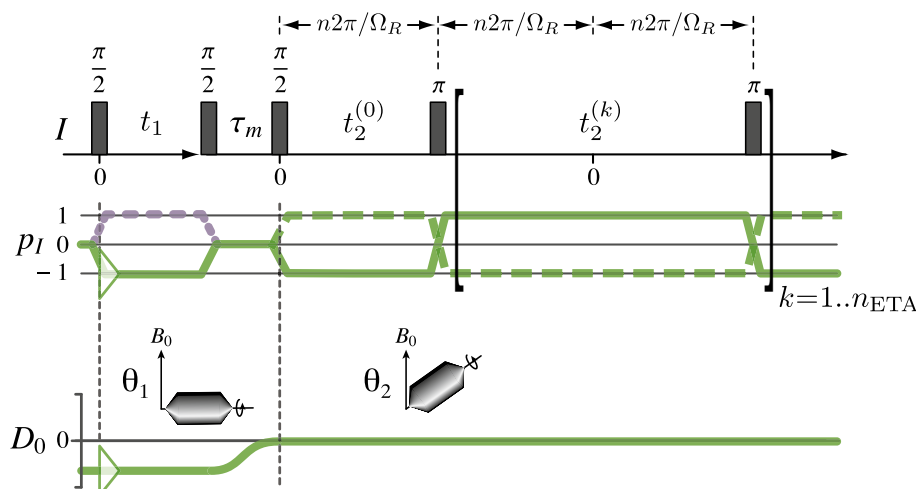


Fig. 2. Magic-angle flipping pulse sequence with echo train acquisition with spin and spatial symmetry pathways. Hypercomplex acquisition is performed to obtain positive and negative t_1 quadrants in the 2D time domain signal [42]. Acquisition parameters are given in Table 3.

given in Table 1. This approach ignores the presence of free oxide (O^{2-}), which is not expected to be present in significant amounts in these silica-rich glass compositions [34].

2.2. NMR measurements

NMR experiments were performed on a hybrid Tecmag Apollo-Chemagnetics CMX II 9.4 T (79.47 MHz for ^{29}Si) NMR spectrometer using either 4 mm or 7 mm rotors in homebuilt dynamic-angle-spinning probes [35]. Rotor packing was performed in a nitrogen-filled glove bag. The sealed rotors were spun with compressed air dried to a dew point of -40°C . Four dummy scans were performed before starting acquisition to establish a steady-state equilibrium and reduce differential relaxation. All experiments were performed at ambient temperature with spinning rates from 12 to 15 kHz for the 4 mm rotor and 6 to 7 kHz for the 7 mm rotor.

The ^{29}Si relaxation time was measured for all glasses using the saturation recovery method [36] under magic-angle spinning (MAS). No evidence of differential relaxation among $Q^{(n)}$ sites was observed in the saturation recovery measurements. The magnetization recovery of the integrated spectrum (i.e., all $Q^{(n)}$ sites) was fit to the stretched exponential function

$$S(t) = S_\infty \cdot [1 - \exp(-t/T_1)^\beta]. \quad (4)$$

Magnetization recovery curves along with best-fit to Eq. (4) are shown in Fig. 1 for two barium silicate glasses with and without CuO doping. A summary of the best-fit parameters are given in Table 2.

The shifted-echo MAF pulse sequence [37,38] used is shown in Fig. 2. This version employs echo-train CPMG acquisition [39–41] and correlates the MAS spectrum with an anisotropic off-magic-angle spectrum. The anisotropic dimension is acquired at an angle, θ_R , nominally perpendicular to the applied field, where the anisotropic frequencies are scaled by a factor of $P_2(\cos \theta_R)$. Further experimental details are given in Table 3 and Fig. 2.

All spectral processing, including affine transformations, were performed with RMN.¹ Following an approach outlined by Dey et al. [41], the MAF signal with echo-train acquisition is converted into a three-dimensional signal with the echo train count, k , forming the third dimension. A matched stretched exponential filter is

applied to the echo train dimension and the 3D signal is projected down to obtain the sensitivity enhanced 2D MAF signal. An active shear of the 2D time domain signal is applied parallel to MAS dimension with a shear ratio of $\kappa = 1$. This leads to a signal correlating pure isotropic and anisotropic dimensions, and leaving all anisotropic cross sections centered at 0 Hz.

2.3. 2D MAF lineshape analysis

In this article we employ the IUPAC definitions for the nuclear shielding and chemical shift interactions [43]. The isotropic nuclear shielding is defined as the trace of the nuclear shielding tensor,

$$\sigma_{\text{iso}} = \frac{1}{3}(\sigma_{zz} + \sigma_{yy} + \sigma_{xx}), \quad (5)$$

where σ_{zz} , σ_{yy} , and σ_{xx} are the components of the second-rank shielding tensor. The isotropic chemical shift is defined as

$$\delta_{\text{iso}} = \frac{\sigma_{\text{ref}} - \sigma_{\text{iso}}}{1 - \sigma_{\text{ref}}}, \quad (6)$$

where, σ_{ref} is the nuclear shielding of the reference compound, TMS for this study.

The nuclear shielding tensor can be visualized as a three-dimensional ellipsoid, and the deviations, positive or negative, of this ellipsoid from a sphere are best understood by examining the elements of the traceless symmetric part of the nuclear shielding tensor, given by

$$S_{ik} = \frac{1}{2}(\sigma_{ik} + \sigma_{ki}) - \sigma_{\text{iso}}. \quad (7)$$

The principal axis system of the second-rank symmetric tensor, \mathbf{S} , is defined as the coordinate system where \mathbf{S} is diagonal with principal components, λ_{zz} , λ_{yy} , and λ_{xx} ordered, according to the Haeberlen convention [43], such that

$$|\lambda_{zz}| > |\lambda_{yy}| > |\lambda_{xx}|. \quad (8)$$

Additionally, we define the second-rank symmetric tensor anisotropy, ζ , and asymmetry parameter, η , according to

$$\zeta_\sigma = \lambda_{zz}, \text{ and } \eta_\sigma = \frac{\lambda_{xx} - \lambda_{yy}}{\zeta_\sigma}. \quad (9)$$

Similarly, following IUPAC convention [43], the notation ζ_δ represents the chemical shift anisotropy, given by

¹ PhySy Ltd, RMN, Version 1.8 (www.physyapps.com, PhySy Ltd, Grandview Heights, OH 43212).

Table 3

Parameters used in pulse sequence of Fig. 2 for 2D MAF-CPMG experiments. Here, n_{ETA} is the number of echoes acquired during echo train acquisition, τ_{rd} is the recycle delay, and τ_{tot} is the total experiment time. The initial t_1 value was 0.1 μs for all compositions. All compositions are doped with approximately 0.5 wt% CuO except $\text{BaO} \cdot 2.75 \text{ SiO}_2$.

Composition	θ_1 (°)	θ_2 (°)	$\frac{\pi}{2}(\theta_1)$ (μs)	τ_m (ms)	$\frac{\pi}{2}(\theta_2)$ (μs)	$n_{t_1} \times n_{t_2}^{(k)}$	Δt_1 (μs)	Δt_2 (μs)	$t_2^{(0)}$ (ms)	$t_2^{(k)}$ (ms)	n_{ETA}	Scans	τ_{rd} (s)	τ_{tot} (h)
$\text{Cs}_2\text{O} \cdot 4.81 \text{ SiO}_2$	87.14	54.74	6.8	183	4.4	64×600	50.0	12.6	3.8	7.6	40	512	9	82.0
$\text{Rb}_2\text{O} \cdot 3.96 \text{ SiO}_2$	90.00	54.74	7.0	183	5.2	77×320	50.0	12.6	2.1	4.1	100	320	5	34.2
$\text{Rb}_2\text{O} \cdot 2.25 \text{ SiO}_2$	90.00	54.74	7.0	183	5.2	80×320	50.0	12.6	2.1	4.1	200	320	6	42.7
$\text{K}_2\text{O} \cdot 4.48 \text{ SiO}_2$	54.74	90.00	9.0	182	3.6	38×160	166.7	25.0	2.1	4.2	50	256	60	162.1
$\text{Na}_2\text{O} \cdot 4.74 \text{ SiO}_2$	87.14	54.74	7.5	183	6.1	66×320	50.0	12.6	2.1	4.1	100	96	14	24.6
$\text{BaO} \cdot 2.64 \text{ SiO}_2$	54.74	90.00	13.0	183	3.6	45×320	125.0	12.6	2.1	4.2	200	48	201	120.6
$\text{BaO} \cdot 2.75 \text{ SiO}_2$	54.74	90.00	8.0	202	3.6	44×120	166.7	25.0	1.6	3.2	80	32	1350	528.0
$\text{SrO} \cdot 2.36 \text{ SiO}_2$	90.00	54.74	7.5	183	6.1	62×320	50.0	12.6	2.1	4.1	100	64	81	89.3

$$\zeta_\delta = -\zeta_\sigma, \quad (10)$$

however, in this article we will keep our discussion in terms of the nuclear shielding anisotropy, ζ_σ .

For the least-squares analysis of each MAF spectrum, a computer program was written using a stochastic Markov chain accepting new steps based on the Metropolis–Hastings criterion in order to ensure the χ^2 minimum was reached [44]. The anisotropic lineshapes are generated in the frequency domain using the POWDER interpolation scheme [45].

For the $Q^{(4)}$ resonances, our model for the 2D MAF spectrum constrains the distribution of isotropic resonance frequencies to follow a skew-normal distribution [46], defined as

$$S(v) = A e^{-\frac{1}{2} \left(\frac{v-\xi}{\Delta} \right)^2} \cdot \left[1 + \text{erf} \left(\frac{\alpha}{\sqrt{2}} \cdot \frac{v-\xi}{\Delta} \right) \right]. \quad (11)$$

The familiar moments of the skew-normal distribution are the mean frequency, \bar{v} , the standard deviation, s , the skewness, γ_1 , and the excess kurtosis, γ_2 . A positive γ_1 signifies a skewed distribution with an asymmetric tail extending out towards positive values, while a negative γ_1 signifies a skewed distribution whose tail extends out toward negative values. The kurtosis, γ_2 , describing the fourth moment of the distribution, is commonly viewed as a measure of the “peakedness” of the distribution and the “weight” of its tail [47].

While the $Q^{(4)}$ resonances in the anisotropic dimension were not expected to have any chemical shift anisotropy, a significant broadening is observed and modeled with a Gaussian distribution. Alternatively, one could use the Czjzek distribution [48]—originally developed to model distributions of electric field gradients in glasses—as a general model for the distribution of second-rank tensor parameters due to random structure variations around an otherwise highly symmetric case like $Q^{(4)}$. However, at low values of the Czjzek distribution parameter, the anisotropic lineshape approaches Gaussian so we chose not to implement this method in our model. Furthermore, we observe that the width of the $Q^{(4)}$ anisotropic broadening varies linearly with increasing isotropic chemical shift. Thus, we model this behavior by constraining the Gaussian line width, Δ , in the anisotropic dimension to depend on the correlated isotropic frequency, v_{iso} , according to

$$\Delta(v_{\text{iso}}) = \Delta_0 + m_{\Delta} \cdot (v_{\text{iso}} - v_{\text{iso,mode}}), \quad (12)$$

where m_{Δ} is the linear slope for the variation of Δ and $v_{\text{iso,mode}}$ is the mode of the $Q^{(4)}$ isotropic lineshape.

For the $Q^{(3)}$ and $Q^{(2)}$ resonances, our model constrains the distribution of isotropic resonance frequencies to follow a normal distribution. Unlike $Q^{(4)}$, no improvements in the least-squares analysis were found on introducing a skew in their isotropic distributions. In the anisotropic dimension the $Q^{(3)}$ and $Q^{(2)}$ resonances were modeled with a Gaussian broadened chemical shift anisotropy lineshape. We also point out that an extended Czjzek model [49–51] has recently been developed as an alternative to model the distribution of second-rank tensor parameters in a glass around first

coordination sphere geometries with well-defined and non-zero anisotropy, such as $Q^{(3)}$, $Q^{(2)}$, and $Q^{(1)}$. Implementing an extended Czjzek model in spectral analysis software, however, is not trivial [52], so we continue to model these random contributions as an additional Gaussian line broadening. In principle, an extended Czjzek model could replace this artificial fit parameter with a more meaningful parameter characterizing longer range disorder in the glass structure.

Based on previous work [23,6,10], the $Q^{(3)}$ resonances were further constrained to be axially symmetric (i.e., $\eta_\sigma = 0$). Based on the results of previous MAF studies on silicate glasses [6,10,7], we also constrain the anisotropy, ζ_σ , and asymmetry parameters, η_σ , to be identical for each $Q^{(n)}$ site in a given glass composition, and no improvements in our least-squares analysis were obtained by releasing this constraint. We use the notation, $\zeta_\sigma^{(n)}$ and $\eta_\sigma^{(n)}$, to represent the nuclear shielding parameters for a $Q^{(n)}$ site.

2.4. Nuclear shielding calculations

The ^{29}Si nuclear shielding tensors were investigated using *Gaussian 03* [53] at B3LYP level with a 6-311++g(2d,p) basis set used for all atoms. Calculations were performed on silicon centered clusters, as shown in Fig. 5, built in the axis system shown to the right of each cluster. The axis not shown in Fig. 5 is positive coming out of the page. These clusters were modeled on a typical $Q^{(4)}$ environment using a Si–O bond distance of 1.61 Å which is based on the bond distance of α -quartz [23,54]. Hydrogens (not shown) were attached to each oxygen and held at a bond angle of 180° in order to preserve the high symmetry of the cluster. The $Q^{(3)}$ cluster was modeled by decreasing the Si–O bond along the z axis of the $Q^{(4)}$ cluster in 0.01 Å steps from 1.61 Å to 1.51 Å. This depression of the Si–O bond distance models the changing Si–NBO bond distance in the presence of different network modifying cation.

3. Results

The dominant nuclear spin relaxation mechanism for natural abundance ^{29}Si in bulk silicate glasses is expected to arise from through-space dipolar couplings to distant rapidly relaxing paramagnetic centers. In this mechanism the ^{29}Si magnetization recovery follows the stretched exponential [55–58] of Eq. (4) with $\beta = 0.5$. As seen in Fig. 1 and Table 2 the addition of paramagnetic dopant to the barium silicate glass provides over an order of magnitude reduction in T_1 from 226 s to 16.4 s with β values falling reasonably close to 0.5. Interestingly, a β value near 0.5 is observed even for the undoped barium silicate glass, suggesting that the relaxation mechanism for this glass arises from dipolar couplings to paramagnetic ions, which likely arise due to trace impurities and defects.

One intriguing observation on examination of T_1 values of all glass compositions in Table 2 is that for the same nominal mole fraction of paramagnetic dopant, the ^{29}Si relaxation times in the alkali silicate glasses are about an order of magnitude shorter than

in the alkaline earth silicate glasses. Since the alkaline earth silicates have a significantly lower density of nuclear magnetic moments compared to the alkali silicates, this suggests that the ^{29}Si relaxation times are also influenced by dipolar couplings to the highly abundant NMR active alkali cation nuclei in the alkali silicate glasses.

To determine the sensitivity gains from combining the strategies of Cu^{2+} doping and echo train acquisition for natural abundance ^{29}Si the 2D MAF spectra were obtained for doped and undoped barium silicate glasses with and without CPMG acquisition. The effect of Cu^{2+} doping on the ^{29}Si relaxation, shown in Table 2, is to reduce the 75% recovery time from 423 s to 33 s. This alone is a factor of 12.8 reduction in total experiment time. Adding CPMG acquisition increases sensitivity by a factor of 2.4 and 2.7 for the doped and undoped barium silicate glasses, respectively. Thus, the combined enhancement yields a factor of 80.6 reduction in total experiment time. It is this combination of echo train acquisition with the better choice of Cu^{2+} as paramagnetic relaxation agent that allowed us to obtain the natural abundance ^{29}Si 2D MAF spectra of the seven different alkali and alkaline-earth glass compositions shown in Fig. 3. One challenge to this approach can be incorporation of the transition metal oxide into the glass composition. While most transition metal oxides are soluble in silicate melts [59–62] there is a risk of volatilization and loss of the paramagnetic metals during synthesis at higher temperatures, particularly in the silica rich compositions. Another concern is whether the oxidation state of the transition metal cation changes when introduced into the melt [62,63].

Recalling the characteristic anisotropic ^{29}Si lineshapes of $Q^{(n)}$ sites [6], the 2D MAF spectra in Fig. 3 confirm and illustrate the well known assignments of ^{29}Si MAS frequencies in silicate glasses: the anisotropic cross-sections correlated to the MAS frequencies between -100 to -110 ppm are dominated by $Q^{(4)}$, the anisotropic cross-sections correlated to the MAS frequencies between -85 to -100 ppm are dominated by $Q^{(3)}$, and only in the strontium silicate composition does the anisotropic dimension reveal a weak $Q^{(2)}$ contribution correlated to MAS frequencies around -80 ppm. Also shown in Fig. 3 are the best-fit 2D lineshapes obtained in our least-squares analyses. The best-fit parameters for the 2D MAF lineshape model, described in Section 2.2, are given in Table 4 for the isotropic chemical shift parameters, and in Table 5 for the anisotropic nuclear shielding parameters. A challenge in presenting uncertainties for the anisotropic shielding parameters arises from a strong covariance with the Gaussian line broadening that is also used in the least-squares analysis of anisotropic lineshapes. The line broadening found during least-squares analysis of the anisotropic cross sections can be attributed to structural disorder, intrinsic excited state lifetime, and uncertainty in the tensor parameters. The uncertainties in the shielding tensor, therefore, can range from values as low as those reported in Table 5 to as high as its corresponding Gaussian line broadening.

The one dimensional projections of the 2D MAF experimental and best-fit spectra onto the isotropic dimension for all glass compositions are shown in Fig. 4. Focusing on the $Q^{(4)}$ isotropic parameters in Table 4 we see that the mean ($\bar{\delta}$) of the $Q^{(4)}$ isotropic resonances span a range of chemical shifts located around -104 ppm to -98 ppm. A well known trend [17] in $Q^{(4)}$ isotropic chemical shift is towards less negative (less shielded) values with increasing network modifier cation potential and with increasing network modifier content as well. A more subtle but established trend is a shift towards less negative values with decreasing Si–O–Si bond angle [64,65]. With the varying silica content and modifier cation potential it is difficult, at first glance, to discern trends in $\bar{\delta}$ in Table 4, but evidence of these trends is present. In the two rubidium silicate glasses there is a shift from -103.0 ppm to

-98.0 ppm with increasing Rb_2O content. The shift in resonance intensity in this range can be assigned to the increasing presence of anionic clusters $Q^{(4,4443)}$, $Q^{(4,4433)}$, $Q^{(4,4333)}$, and $Q^{(4,3333)}$ with increasing network modifier, consistent with observations in double quantum experiments [66–68]. Additionally, we see a marked shift of $\bar{\delta}$ from -101.3 ppm to -98.0 ppm in comparing $\text{SrO} \cdot 2.36 \text{SiO}_2$ to $\text{Rb}_2\text{O} \cdot 2.25 \text{SiO}_2$, respectively.

The standard deviation of the isotropic $Q^{(4)}$ resonance distribution is approximately 5.5 ppm for the alkali silicates and 6 ppm for the alkaline earth silicates. The larger isotropic spread in the alkaline earth silicates are a reflection of the more random distribution of anionic species caused by the higher cation potentials of Ba and Sr. We also found that incorporating skewness into our lineshape model gave improvement in the least-squares analysis for $Q^{(4)}$ resonances but not $Q^{(3)}$ or $Q^{(2)}$. Even then, we find the skewness and excess kurtosis of the $Q^{(4)}$ isotropic lineshape, as shown in Table 4, were near zero in all glasses except $\text{Cs}_2\text{O} \cdot 4.81 \text{SiO}_2$ and $\text{SrO} \cdot 2.36 \text{SiO}_2$. It seems odd that these $Q^{(4)}$ lineshape asymmetries occur in the two glass compositions with the most different modifier cation potentials in this study. The asymmetry in the lineshape, however, is subtle and we hesitate to speculate on its origins without further experimental data.

While it is often the first coordination sphere geometry that determines the second-rank anisotropy, there are situations where the first coordination sphere geometry has a symmetry that leads to no anisotropy. Such is the case with the tetrahedral symmetry around ^{29}Si in $Q^{(4)}$ sites. Thus, the origin of the observed ^{29}Si anisotropy in $Q^{(4)}$ likely arises from random structural deviations away from this high symmetry in the first- and higher-coordination spheres of silicon. We have found the anisotropic lineshape of the $Q^{(4)}$ sites is well modeled with a Gaussian lineshape that increases in width with increasing isotropic chemical shift. We explain this increasing anisotropic width by assigning the narrowest anisotropic cross-sections at the most negative chemical shifts to $Q^{(4,4444)}$ sites. As we move to more positive chemical shifts, the Gaussian width of the anisotropic cross-section increases, though no characteristic powder lineshape is observed. Again, this behavior is consistent with our assignment of these $Q^{(4)}$ resonance frequencies in anionic clusters with $Q^{(3)}$, such as $Q^{(4,4443)}$, $Q^{(4,4433)}$, $Q^{(4,4333)}$, and $Q^{(4,3333)}$.

Shifting our attention to the $Q^{(3)}$ isotropic parameters we note that the mean ($\bar{\delta}$) of the $Q^{(3)}$ isotropic resonances span a narrower range of chemical shifts than $Q^{(4)}$, located around -94 ppm to -89 ppm, and similarly shift towards more positive chemical shift values with increasing network modifier content. Again, the increase in $Q^{(3)}$ isotropic resonances at the more positive chemical shift values with increasing modifier content can analogously be assigned to the presence of anionic cluster $Q^{(3,4444)}$, $Q^{(3,4433)}$, $Q^{(3,4333)}$, and $Q^{(3,3333)}$. The standard deviation of the isotropic resonances are around 4 ppm for the alkali silicates, and 5–6 ppm for alkaline earth silicates. Again, the larger spread in the alkaline earth silicates are a reflection of the more random anionic species distribution caused by the higher cation potentials of Ba and Sr.

Only in the strontium silicate glass composition do the 2D MAF spectra reveal the presence of $Q^{(2)}$ sites. We observe no evidence of $Q^{(1)}$ or $Q^{(0)}$ sites in any glass composition in this study. This also suggests there is no significant free oxide (O^{2-}) in the barium and strontium silicate glasses above the disilicate composition. The observed $Q^{(2)}$ isotropic resonance frequencies are shifted towards more positive chemical shifts with a greater isotropic spread than the $Q^{(3)}$ resonance.

Given the relative areas from the 2D MAF spectrum analysis in Table 4 for the $Q^{(2)}$, $Q^{(3)}$, and $Q^{(4)}$ sites in the strontium silicate glass and the assumption that the following anionic equilibria [69,70] takes place in the melt:

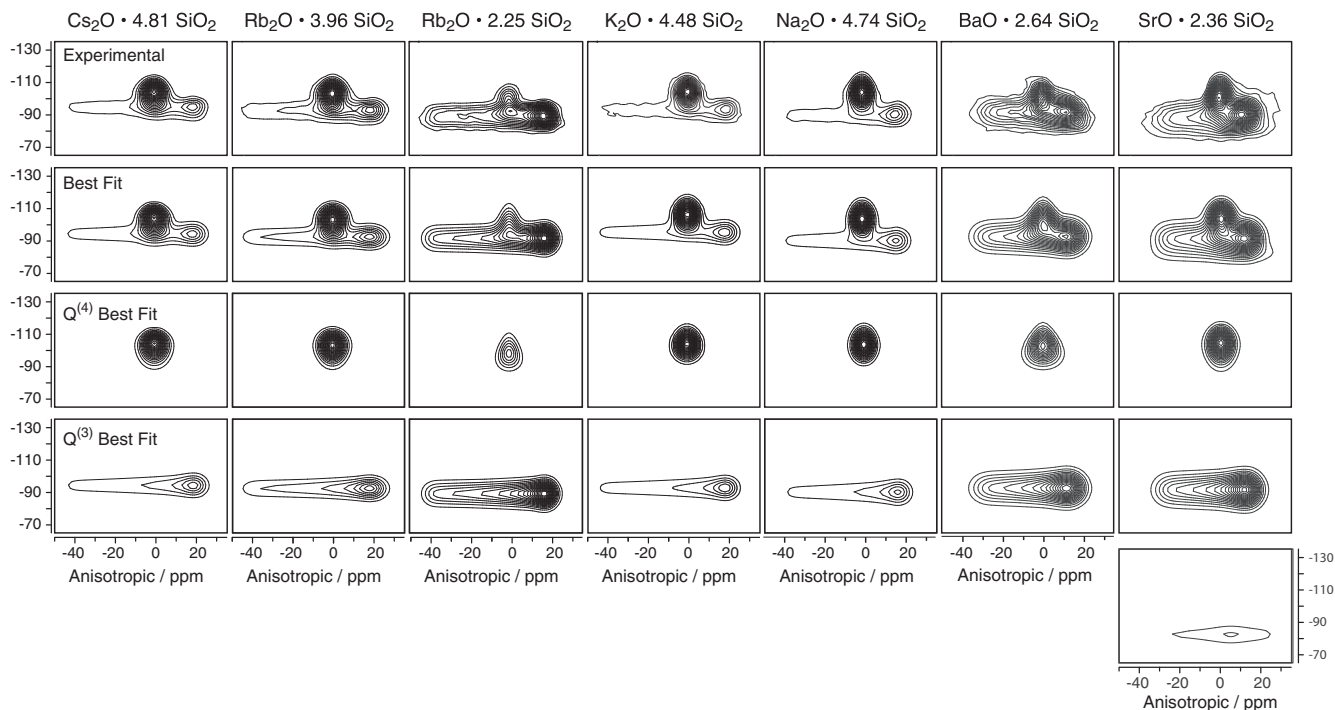


Fig. 3. Experimental 2D MAF spectra (first row) of $\text{Cs}_2\text{O} \cdot 4.81 \text{SiO}_2$, $\text{Rb}_2\text{O} \cdot 3.96 \text{SiO}_2$, $\text{Rb}_2\text{O} \cdot 2.25 \text{SiO}_2$, $\text{K}_2\text{O} \cdot 4.48 \text{SiO}_2$, $\text{Na}_2\text{O} \cdot 4.74 \text{SiO}_2$, $\text{BaO} \cdot 2.64 \text{SiO}_2$, $\text{SrO} \cdot 2.36 \text{SiO}_2$ with best fit spectra (second row), best fit $Q^{(4)}$ site (third row), best fit $Q^{(3)}$ site (fourth row) and best fit $Q^{(2)}$ site (last row). The averaged reduced χ^2 are 1.36, 1.59, 1.50, 1.40, 1.26, 1.35 and 2.42 respectively. Twenty equally spaced contours are plotted from 5% to 95% of the maximum intensity. All frequencies (in ppm) are referenced to TMS.

$$2Q^{(3)} = Q^{(2)} + Q^{(4)}, \quad (13)$$

we can calculate the corresponding equilibrium constant,

$$k_3 = \frac{x_{Q_4} x_{Q_2}}{(x_{Q_3})^2}, \quad (14)$$

where x_{Q_n} is the mole fraction of the $Q^{(n)}$ species. From k_3 one can infer how the $Q^{(n)}$ anions are distributed in the bulk glass. When k_3 is zero the distribution of silicate tetrahedra within the glass is binary, that is, the glass contains a maximum of two $Q^{(n)}$ -species with the sequential appearance of other $Q^{(n)}$ -species as the modifier cation content increases [71]. In contrast, calculated values of k_3 , assuming a statistically random distribution and neglecting the formation of free oxygen anion, would give $k_3 = 0.375$ [72]. Thus, one can view the equilibrium constants as a measure of frozen-in disorder or configurational entropy of the glass. In a glass with composition $\gamma\text{MO} \cdot (1 - \gamma)\text{SiO}_2$ the mole fractions of all species in the equilibria of Eq. (13) are calculated [11] according to

$$x_{Q_n} = \frac{y_{Q_n}}{\left(\frac{\gamma}{1-\gamma}\right) - y_{Q_0} - 0.5y_{Q_1} + 0.5y_{Q_3} + y_{Q_4}}. \quad (15)$$

Using the expression above with the ^{29}Si NMR relative $Q^{(n)}$ abundances given in Table 4, the k_3 values of $k_3^{(\text{Sr})} = 0.058 \pm 0.006$ for the $\text{SrO} \cdot 2.36\text{SiO}_2$ glass. This value is in line with the trend in k_3 (Fig. 7 in Ref. [11]) with increasing cation potential observed by Davis et al. [11].

4. Discussion

The primary focus of this study is to examine the dependence of the ^{29}Si shielding anisotropy of $Q^{(3)}$ sites on modifier cation. Based on our previous ^{29}Si MAF measurements in alkali and alkaline earth silicate glasses [6,7,10,11], we noted a systematic decrease

in the ^{29}Si shielding anisotropy with increasing modifier cation potential [11]. In combination with these previous studies, the seven glass compositions in this study were chosen to explore a wider variety of modifier cations. The ^{29}Si shielding anisotropy of $Q^{(3)}$ variations for the seven glass compositions in this study, along with previous works, are given in Table 5. The variation in the ^{29}Si shielding anisotropy of $Q^{(3)}$ ranges from 27 ppm for Mg to approximately 90 ppm for Cs and K. As noted in the Introduction the origin of this trend was explained by Grimmer and coworkers [73,22,23] and Kirkpatrick and coworkers [26,74,27,75] who noted a linear relationship between the ^{31}P nuclear shielding anisotropy and the P–O bond length in a number of phosphorus compounds [73] and crystalline orthophosphates [26].

To better illustrate the linear relationship between the ^{29}Si shielding and the Si–NBO bond length, we performed ab initio calculations on $\text{Si}(\text{OH})_4$ clusters modeling $Q^{(n)}$ tetrahedra. In these calculations we chose a coordinate system with the z axis along the Si–NBO bond and one Si–BO bond in the z–y plane, as illustrated in Fig. 5. The $Q^{(4)}$ on the right with all Si–BO distances equal has a spherical ^{29}Si shielding tensor ($\sigma_{xx} = \sigma_{yy} = \sigma_{zz}$). A $Q^{(3)}$ is modeled on the left by compressing the Si–O bond along z, resulting in a prolate spheroid ($\sigma_{xx} = \sigma_{yy} < \sigma_{zz}$) shielding tensor. As seen in Fig. 5A, this causes the nuclear shielding to become more shielded along the z axis due to a corresponding increase in electron density along the Si–NBO bond, while becoming less shielded along the x and y axes. Since the decrease in shielding perpendicular to the compressed Si–O bond is slightly greater in magnitude than the increase in shielding along the compressed Si–O bond, the isotropic shielding, shown as a solid line in Fig. 5A, decreases as the Si–O bond is compressed, consistent with well known trends for isotropic ^{29}Si chemical shifts [76]. Of greater relevance to this study are the symmetric tensor elements, S_{ii} , of the ^{29}Si nuclear shielding tensor as a function of Si–NBO distance shown in Fig. 5B. The S_{zz} value, which is the nuclear shielding anisotropy, ζ_σ , for the cluster, becomes smaller as the Si–NBO bond distance increases towards

Table 4
Best fit parameters area (ν_{area}), skewness (γ_1), and excess kurtosis (γ_2) for the isotropic dimension for each $Q^{(n)}$ site obtained from the least-squares analysis of 2D MAF spectra in Fig. 3. The shape parameter, z , in the skew-normal distribution was constrained to a value of zero (i.e., normal distribution) for $Q^{(3)}$ and $Q^{(2)}$ resonances. Parameter uncertainties are given as 2.58 times one standard deviation (99% confidence limit). All compositions are doped with approximately 0.5 wt% CuO except BaO · 2.75 SiO₂.

Composition	$Q^{(4)}$				$Q^{(3)}$				$Q^{(2)}$			
	ν_{area}^4 (%)	$\bar{\delta}$ (ppm)	s (ppm)	γ_1	γ_2	ν_{area}^3 (%)	$\bar{\delta}$ (ppm)	s (ppm)	ν_{area}^2 (%)	$\bar{\delta}$ (ppm)	s (ppm)	z (ppm)
Cs ₂ O · 4.81 SiO ₂	58.4 ± 0.3	-102.3 ± 0.7	5.45 ± 0.10	0.50 ± 0.02	0.35 ± 0.02	41.6 ± 0.4	-94.3 ± 0.7	4.05 ± 0.08	-	-	-	-
Rb ₂ O · 3.96 SiO ₂	49.5 ± 0.2	-103.0 ± 0.7	5.28 ± 0.05	0.00001 ± 0.00001	0.0 ± 0.0	50.5 ± 0.2	-92.7 ± 0.7	4.15 ± 0.04	-	-	-	-
Rb ₂ O · 2.25 SiO ₂	11.0 ± 0.3	-98.0 ± 0.7	5.64 ± 0.19	0.0003 ± 0.0003	0.0 ± 0.0	89.0 ± 0.1	-89.5 ± 0.7	4.65 ± 0.05	-	-	-	-
K ₂ O · 4.48 SiO ₂	55.3 ± 0.1	-103.8 ± 0.7	5.15 ± 0.02	0.0017 ± 0.0001	0.0 ± 0.0	44.7 ± 0.1	-92.9 ± 0.7	4.19 ± 0.02	-	-	-	-
Na ₂ O · 4.74 SiO ₂	57.8 ± 0.1	-103.7 ± 0.7	5.31 ± 0.03	0.0010 ± 0.0001	0.0 ± 0.0	42.2 ± 0.2	-90.5 ± 0.7	4.29 ± 0.04	-	-	-	-
BaO · 2.64 SiO ₂	24.3 ± 3.0	-99.8 ± 0.8	6.06 ± 0.39	0.021 ± 0.005	0.005 ± 0.002	75.7 ± 0.8	-90.8 ± 0.7	5.72 ± 0.16	-	-	-	-
BaO · 2.75 SiO ₂	27.2 ± 0.7	-101.2 ± 0.7	6.20 ± 0.17	0.022 ± 0.004	0.005 ± 0.001	72.8 ± 0.6	-90.8 ± 0.7	5.83 ± 0.12	-	-	-	-
SrO · 2.36 SiO ₂	25.1 ± 0.8	-101.3 ± 0.8	6.27 ± 0.28	0.29 ± 0.03	0.16 ± 0.02	65.1 ± 0.6	-89.9 ± 0.7	5.68 ± 0.16	9.8 ± 0.9	-80.9 ± 0.9	3.52 ± 0.16	-

the Si–BO bond length. Admittedly, this simple computational model ignores the influence of higher coordination spheres; however, it provides the correct explanation for the observed trends.

Given this fundamental and linear relationship between the Si–NBO bond length and ζ_{σ} , how might one explain the observed experimental correlation in Fig. 6 between ζ_{σ} and the nature of the network modifier cation? There is a well established linear relationship between bond length and electronegativity differences [77–81]. Assuming that the Si electronegativity remains constant, we can attribute the variations in the Si–NBO length to changes in the NBO electronegativity. These changes, in turn, arise from coordination of the NBO by varying number of network modifying cations with varying electronegativity. Thus, the approximate linear dependence of ζ_{σ} on network modifier cation potential in Fig. 6 would imply a direct proportionality between a network modifier cation's electronegativity and its potential—a relationship consistent with the electronegativity definition of Gordy [79].

Given the explanation above, there is a clear need for additional work to calibrate the relationship between ²⁹Si nuclear shielding anisotropy and Si–NBO bond lengths in $Q^{(n)}$ sites. This can be done empirically, through solid-state NMR measurements of shielding tensors in crystalline materials of known structure. This approach has been successful with calibrating the ³¹P nuclear shielding tensors [73,26] in phosphates and, analogously, the ¹⁷O efg tensor with bond lengths and angles around oxygen in silicates [83–87]. Alternatively, first-principle quantum chemical calculations [88] on crystalline silicates of known structure could also be brought to bear on this issue. Interestingly, the results of Fig. 6 also suggests that the ¹⁷O quadrupolar coupling constant, C_q , of the NBO, which is known to vary linearly with Si–O length [89,90], would also be a probe of variations in the modifier coordination environments around non-bridging oxygen. It may be that this indirect effect of modifier cation potential on the Si–NBO length plays a larger role in variations of the NBO ¹⁷O C_q value than the direct perturbation of the NBO electric field gradient by the spatial distribution of modifier cation charges.

Finally, another intriguing observation in Fig. 6 is that increasing modifier concentration causes the anisotropy to decrease when going from K₂O · 4.48 SiO₂ to K₂O · 2 SiO₂ and from Na₂O · 4.74 SiO₂ to 2Na₂O · 3 SiO₂. These differences of ~10 ppm are greater than our measurement uncertainty. One possible explanation alluded to earlier is that the $Q^{(3)}$ Si–NBO length is increasing with increasing coordination of the NBO by the modifier cations. This structural picture is analogous to the proposed structural changes in the distinct compositional ranges of Hoppe [91] proposed in phosphate glasses. That is, in high silica compositions the non-bridging oxygen could be coordinated by smaller clusters of modifier cations, which would have a weaker pull on the Si–NBO length. In turn, as the network modifier concentration increases, the number of modifier cations clustered around the non-bridging oxygen increases [92,93], causing the Si–NBO bond to lengthen, as illustrated below.

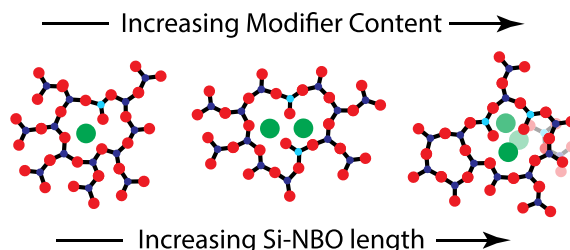


Table 5
Best fit parameters for the nuclear shielding anisotropy parameters, ζ_σ and η_σ , and GB is the standard deviation of Gaussian line broadening for each $Q^{(n)}$ obtained from least-squares analysis 2D MAF spectra in Fig. 3. The value of η_σ was constrained to a value of zero for $Q^{(3)}$ resonances. Parameter uncertainties are given as 2.58 times one standard deviation (99% confidence limit). All compositions are doped with approximately 0.5 wt% CuO except BaO · 2.75 SiO₂.

Composition	$Q^{(4)}$		$Q^{(3)}$		$Q^{(2)}$		η_σ	GB (ppm)	Ref.
	Δ_0 (ppm)	m_Δ	ζ_σ (ppm)	η_σ	GB (ppm)	ζ_σ (ppm)			
Cs ₂ O · 4.81 SiO ₂	4.31 ± 0.02	0.042 ± 0.002	89.7 ± 0.6	0	7.8	–	–	–	This work
Rb ₂ O · 3.96 SiO ₂	3.81 ± 0.02	0.011 ± 0.001	87.9 ± 0.5	0	9.2 ± 0.3	–	–	–	This work
Rb ₂ O · 2.25 SiO ₂	3.93 ± 0.12	0.088 ± 0.011	80.7 ± 0.4	0	6.7 ± 0.2	–	–	–	This work
K ₂ O · 4.48 SiO ₂	3.50 ± 0.01	0.023 ± 0.001	88.8 ± 0.2	0	7.6 ± 0.1	–	–	–	This work
Na ₂ O · 4.74 SiO ₂	3.77 ± 0.01	0.046 ± 0.001	79.8 ± 0.4	0	7.1 ± 0.3	–	–	–	This work
BaO · 2.64 SiO ₂	4.46 ± 0.36	0.130 ± 0.048	63.4 ± 1.0	0	9.6 ± 0.7	–	–	–	This work
BaO · 2.75 SiO ₂	4.46 ± 0.12	0.048 ± 0.011	62.6 ± 0.8	0	11.1 ± 0.7	–	–	–	This work
SrO · 2.36 SiO ₂	3.79 ± 0.12	0.028 ± 0.008	59.8 ± 0.7	0	9.2	66.2	0.71 ± 0.04	9.9	This work
K ₂ O · 2 SiO ₂	–	–	74.9 ± 0.2	0.030 ± 0.006	–	85.0 ± 1.3	0.48 ± 0.02	–	[10]
2Na ₂ O · 3 SiO ₂	–	–	69	0.03	–	78.0	0.53	–	[6]
CaO · SiO ₂	–	–	45.4	0.01	–	48.3	0.70	–	[7]
MgO · SiO ₂	–	–	27.5 ± 0.5	0.45 ± 0.11	–	36.0 ± 0.5	0.99 ± 0.07	–	[11]

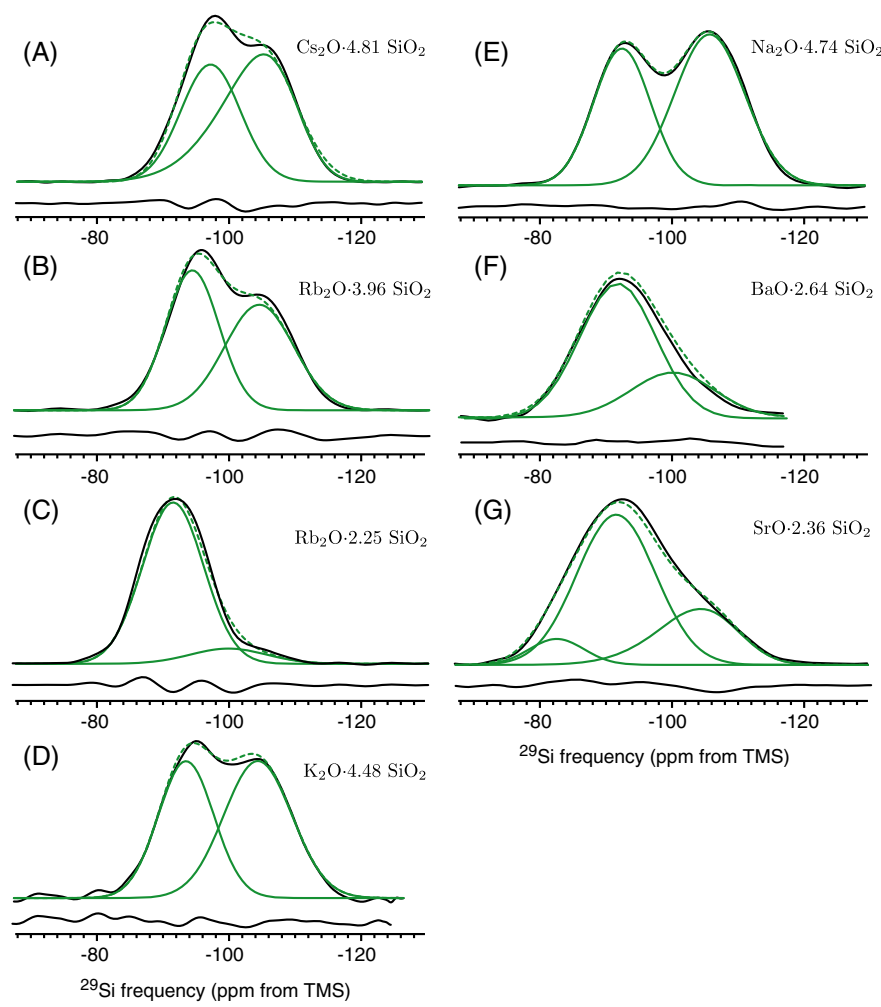


Fig. 4. One dimensional projections of 2D MAF experimental and best-fit spectra onto the isotropic dimension for glass compositions (A) Cs₂O · 4.81 SiO₂, (B) Rb₂O · 3.96 SiO₂, (C) Rb₂O · 2.25 SiO₂, (D) K₂O · 4.48 SiO₂, (E) Na₂O · 4.74 SiO₂, (F) BaO · 2.64 SiO₂, (G) SrO · 2.36 SiO₂. Also shown in each plot is the difference between the experimental and best-fit projections. Best-fit parameters are given in Table 4. Dashed lines represents the one dimensional projections of the best-fit 2D MAF spectra. Also shown are one dimensional projections of $Q^{(n)}$ components of the best-fit 2D MAF spectra. The $Q^{(4)}$, $Q^{(3)}$, and $Q^{(2)}$ components appear from right to left, respectively, at progressively higher chemical shifts.

This trend of increasing Si–NBO length with increasing modifier content is also consistent with recent molecular dynamics simulations in alkali silicate glasses [94,95]. Further natural abundance ²⁹Si MAF studies exploring these variations of ²⁹Si shielding anis-

otropy of $Q^{(n)}$ species in a systematic variation of mole fraction in γ M₂O · (1 – γ)SiO₂ glass compositions is underway in our laboratory.

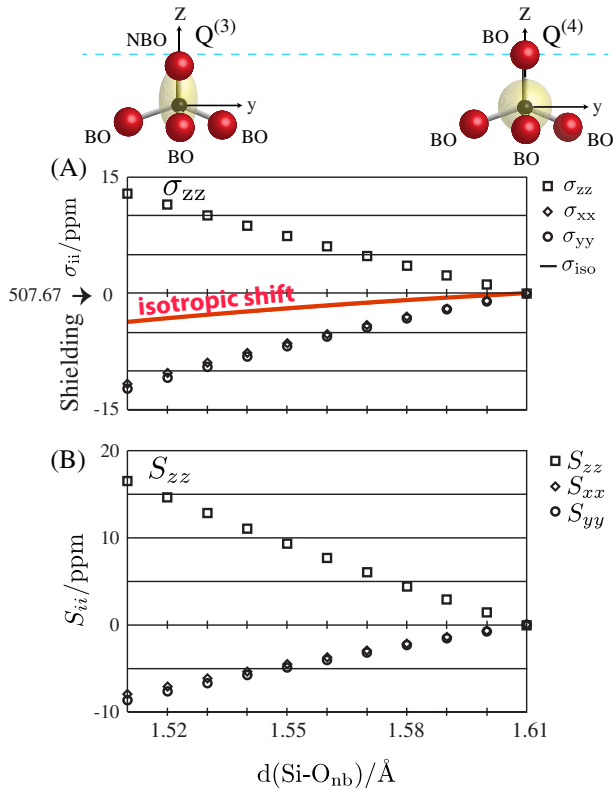


Fig. 5. Ab initio results for $Q^{(1)}$ and $Q^{(3)}$ clusters as a function of Si-NBO distance with all Si-BO distances constant at 1.61 Å. (A) Full shielding tensor components and (B) symmetric part of the shielding tensor in the indicated molecular coordinate system.

5. Summary

We show that Cu^{2+} is a good choice as a paramagnetic relaxation agent for echo train acquisition in glasses as it reduces T_1 , i.e., recycle delays, without significant reductions in T_2 . The combination of Cu^{2+} as a paramagnetic dopant with echo train acquisition allows us to perform natural abundance (4.7%) ^{29}Si MAF measurements with an order of magnitude enhancement in sensitivity.

We exploit this sensitivity enhancement in a systematic investigation of the natural abundance two-dimensional ^{29}Si Magic-Angle Flipping spectra of a series of alkali and alkaline-earth silicate glasses and measure the relative populations of $Q^{(n)}$ anionic species present in each glass with much higher precision than can be obtained from one-dimensional Magic-Angle Spinning measurements. The assumption of a Gaussian distribution of isotropic ^{29}Si chemical shifts for the $Q^{(n)}$ anionic species was found to be valid in all compositions with the exception of a slight skewness in the $Q^{(4)}$ resonance of $\text{Cs}_2\text{O} \cdot 4.81 \text{ SiO}_2$ and $\text{SrO} \cdot 2.36 \text{ SiO}_2$ glasses. From the calculated mole fractions the $Q^{(3)}$ disproportionation constant, k_3 , for $\text{SrO} \cdot 2.36 \text{ SiO}_2$ glass was obtained for the first time. No evidence for $Q^{(1)}$ nor $Q^{(0)}$ species were detected in their MAF spectra. Similarly, no evidence for $Q^{(2)}$, $Q^{(1)}$ nor $Q^{(0)}$ species were detected in the MAF spectra $\text{BaO} \cdot 2.64 \text{ SiO}_2$ glass and $\text{BaO} \cdot 2.75 \text{ SiO}_2$ glass suggesting no free oxide is present in significant amounts in these alkaline earth silicate glass compositions.

Fits of anisotropic cross sections of the ^{29}Si 2D MAF spectrum allowed the nuclear shielding parameters for $Q^{(3)}$ to be determined, and the observed $\zeta_\sigma^{(3)}$ values were consistent with trends reported in a previous MAF studies [6,7,10,11] where the magnitude of ζ_σ is observed to decrease as the cation potential increases. Based on results of Grimmer and coworkers [22,23], this trend of ζ_σ versus cation potential indicates the increased ability of smaller more highly charged cations, such as Mg^{2+} , to withdraw electron density from the ^{29}Si nucleus as the Si-NBO bond length increases, ultimately approaching a bridging Si-O-Si bond. Additionally, we observe a systematic decrease in $\zeta_\sigma^{(3)}$ with increasing modifier

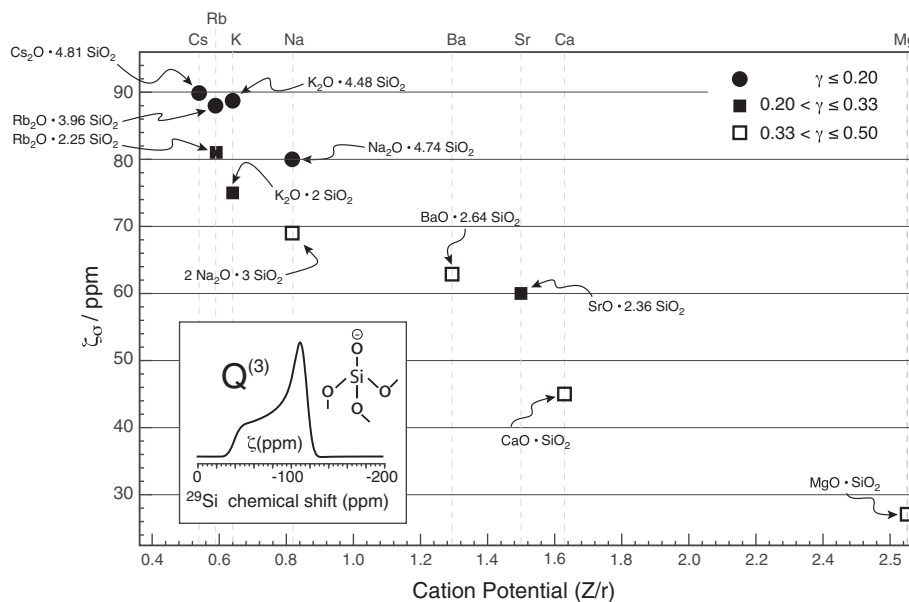


Fig. 6. Plot of ζ_σ versus cation potential for $Q^{(3)}$. In addition to the seven $\zeta_\sigma^{(3)}$ values from this work, the $\zeta_\sigma^{(3)}$ values of $\text{K}_2\text{O} \cdot 2 \text{ SiO}_2$ [10], $2\text{Na}_2\text{O} \cdot 3 \text{ SiO}_2$ [6], $\text{CaO} \cdot \text{SiO}_2$ [7] and $\text{MgO} \cdot \text{SiO}_2$ [11] from previous studies are presented [7]. The γ is the mole fraction of modifier oxide from $\gamma\text{M}_2\text{O} \cdot (1 - \gamma)\text{SiO}_2$, where $z = 1$ or 2, sample, and is grouped into three ranges. Z is the charge of coordinating cation and r is the atomic radii [82]. For each sample, the smallest radius was used to calculate Z/r_{max} and the largest radius was used to calculate Z/r_{min} . The average of Z/r_{max} and Z/r_{min} was used in the plot because of the presence of multiple radii resulted from different coordination numbers for each cation.

cation concentration. This suggests that larger clusters of network modifier cations will also lengthen the Si–NBO bond length and lead to smaller $\zeta_{\sigma}^{(3)}$ values.

Such experiments are important parts of a collective multi-dimensional NMR strategy that, as Mattias Edén notes in his recent review [13], has been “only exploited to a minor fraction of its full potential” in characterizing intermediate range structure in glasses. This information is valuable in testing predictive models for structure–property relationships in glasses [96], such as topological constraint theory [97–101] and the related temperature-dependent constraint theory [102,103], where one needs to know enough about the structure of a given glass to identify relevant structural units and constraints; the best source of this kind of structural detail can come from experimental NMR measurements [104–107].

Acknowledgments

This material is based upon work supported in part by the USA National Science Foundation under Grants No. CHE-1506870 and CHE-1012175. The authors thank Dr. Brennan Walder and Professor Christopher Jaroniec for helpful discussions.

Appendix A. Supplementary material

Supplementary data associated with this article can be found, in the online version, at <http://dx.doi.org/10.1016/j.jmr.2016.05.003>.

References

- [1] E.A. Porai-Koshits, Genesis of concepts on structure of inorganic glasses, *J. Non-Cryst. Solids* 123 (1990) 1–13, [http://dx.doi.org/10.1016/0022-3093\(90\)90767-G](http://dx.doi.org/10.1016/0022-3093(90)90767-G).
- [2] A. Wright, Neutron scattering from vitreous silica. V. The structure of vitreous silica: What have we learned from 60 years of diffraction studies?, *J. Non-Cryst. Solids* 179 (1994) 84–115, [http://dx.doi.org/10.1016/0022-3093\(94\)90687-4](http://dx.doi.org/10.1016/0022-3093(94)90687-4).
- [3] G.N. Greaves, S. Sen, Inorganic glasses, glass-forming liquids and amorphizing solids, *Adv. Phys.* 56 (2007) 1–166, <http://dx.doi.org/10.1080/00018730601147426>.
- [4] I. Farnan, P.J. Grandinetti, J.H. Baltisberger, J.F. Stebbins, U. Werner, M.A. Eastman, A. Pines, Quantification of the disorder in network-modified silicate glasses, *Nature* 358 (1992) 31–35, <http://dx.doi.org/10.1038/358031a0>.
- [5] P. Florian, K.E. Vermillion, P.J. Grandinetti, I. Farnan, J.F. Stebbins, Cation distribution in mixed alkali disilicate glasses, *J. Am. Chem. Soc.* 118 (1996) 3493–3497, <http://dx.doi.org/10.1021/ja953918c>.
- [6] P. Zhang, C. Dunlap, P. Florian, P.J. Grandinetti, I. Farnan, J.F. Stebbins, Silicon site distributions in an alkali silicate glass derived by two-dimensional ^{29}Si nuclear magnetic resonance, *J. Non-Cryst. Solids* 204 (1996) 294–300, [http://dx.doi.org/10.1016/S0022-3093\(96\)00601-1](http://dx.doi.org/10.1016/S0022-3093(96)00601-1).
- [7] P. Zhang, P.J. Grandinetti, J.F. Stebbins, Anionic species determination in CaSiO_3 glass using two-dimensional ^{29}Si NMR, *J. Phys. Chem. B* 101 (20) (1997) 4004–4008, <http://dx.doi.org/10.1021/jp9700342>.
- [8] P. Zhang, A.N. Klymchyov, S. Brown, J.G. Ellington, P.J. Grandinetti, Solid-state ^{13}C NMR investigations of the glycosidic linkage in α -D-trehalose, *Solid State NMR* 12 (1998) 221–225, [http://dx.doi.org/10.1016/S0926-2040\(98\)00069-1](http://dx.doi.org/10.1016/S0926-2040(98)00069-1).
- [9] T.M. Clark, P.J. Grandinetti, P. Florian, J.F. Stebbins, Correlated structural distributions in silica glass, *Phys. Rev. B* 70 (2004) 064202, <http://dx.doi.org/10.1103/PhysRevB.70.064202>.
- [10] M. Davis, D.C. Kaseman, S.M. Parvani, K.J. Sanders, P.J. Grandinetti, P. Florian, D. Massiot, $Q^{(n)}$ -species distribution in K_2O 2SiO_2 by ^{29}Si magic angle flipping NMR, *J. Phys. Chem. A* 114 (17) (2010) 5503–5508, <http://dx.doi.org/10.1021/jp100530m>.
- [11] M. Davis, K.J. Sanders, P.J. Grandinetti, S.J. Gaudio, S. Sen, Structural investigations of magnesium silicate glasses by ^{29}Si magic-angle flipping NMR, *J. Non-Cryst. Solids* 357 (2011) 2787–2795, <http://dx.doi.org/10.1016/j.jnoncrsol.2011.02.045>.
- [12] H. Eckert, Structural characterization of noncrystalline solids and glasses using solid state NMR, *Prog. NMR Spectrosc.* 24 (1992) 159, [http://dx.doi.org/10.1016/0079-6565\(92\)80001-V](http://dx.doi.org/10.1016/0079-6565(92)80001-V).
- [13] M. Edén, NMR studies of oxide-based glasses, *Annu. Rep. Prog. Chem., Sect. C: Phys. Chem.* 108 (2012) 177–221, <http://dx.doi.org/10.1039/C2PC90006H>.
- [14] J.B. Murdoch, J.F. Stebbins, I.S.E. Carmichael, High-resolution ^{29}Si NMR study of silicate and aluminosilicate glasses: the effect of network-modifying cations, *Am. Mineral.* 70 (1985) 332–343.
- [15] E. Schneider, J.F. Stebbins, A. Pines, Speciation and local structure in alkali and alkaline earth silicate glasses: constraints from ^{29}Si NMR spectroscopy, *J. Non-Cryst. Solids* 89 (1987) 371–383, [http://dx.doi.org/10.1016/S0022-3093\(87\)80279-X](http://dx.doi.org/10.1016/S0022-3093(87)80279-X).
- [16] R. Dupree, D. Holland, P.W. McMillan, R.F. Pettifer, The structure of soda-silica glasses: a MAS NMR study, *J. Non-Cryst. Solids* 68 (1984) 399, [http://dx.doi.org/10.1016/0022-3093\(84\)90020-6](http://dx.doi.org/10.1016/0022-3093(84)90020-6).
- [17] H. Maekawa, T. Maekawa, K. Kawamura, T. Yokokawa, The structural groups of alkali silicate glasses determined from ^{29}Si MAS-NMR, *J. Non-Cryst. Solids* 127 (1991) 53–64, [http://dx.doi.org/10.1016/0022-3093\(91\)90400-Z](http://dx.doi.org/10.1016/0022-3093(91)90400-Z).
- [18] J.F. Emerson, P.E. Stallworth, P.J. Bray, High-field ^{29}Si NMR studies of alkali silicate glasses, *J. Non-Cryst. Solids* 113 (1989) 253, [http://dx.doi.org/10.1016/0022-3093\(89\)90019-7](http://dx.doi.org/10.1016/0022-3093(89)90019-7).
- [19] A.-R. Grimmer, M. Magi, M. Hahnert, H. Stade, A. Samoson, W. Wieker, E. Lippmaa, High-resolution solid-state ^{29}Si nuclear magnetic resonance spectroscopic studies of binary alkali silicate-glasses, *Phys. Chem. Glasses* 25 (4) (1984) 105–109.
- [20] C.M. Schramm, B.H.W.S.d. Jong, V.E. Parziale, ^{29}Si magic angle spinning NMR study on local silicon environments in amorphous and crystalline lithium silicates, *J. Am. Chem. Soc.* 106 (1984) 4396.
- [21] J.F. Stebbins, Identification of multiple structural species in silicate glasses by ^{29}Si NMR, *Nature* 330 (1987) 465, <http://dx.doi.org/10.1038/330465a0>.
- [22] A.-R. Grimmer, E.F. Gechner, G. Molgedey, High resolution ^{29}Si NMR in solid silicates. correlations between shielding tensor and Si–O bond length, *Chem. Phys. Lett.* 77 (1981) 331–335, [http://dx.doi.org/10.1016/0009-2614\(81\)80158-3](http://dx.doi.org/10.1016/0009-2614(81)80158-3).
- [23] A.-R. Grimmer, Correlation between individual Si–O bond lengths and the principal values of the ^{29}Si chemical-shift tensor in solid silicates, *Chem. Phys. Lett.* 119 (1985) 416–420, [http://dx.doi.org/10.1016/0009-2614\(85\)80446-2](http://dx.doi.org/10.1016/0009-2614(85)80446-2).
- [24] A. Bax, N.M. Szevenyi, G.E. Maciel, Chemical shift anisotropy in powdered solids studied by 2D FT NMR with flipping of the spinning axis, *J. Magn. Reson.* 55 (1983) 494.
- [25] T. Terao, T. Fujii, T. Onodera, A. Saika, Switching-angle sample-spinning NMR spectroscopy for obtaining powder-pattern-resolved 2D spectra: measurements of ^{13}C chemical-shift anisotropies in powdered 3,4-dimethoxybenzaldehyde, *Chem. Phys. Lett.* 107 (1984) 145.
- [26] G.L. Turner, K.A. Smith, R. Kirkpatrick, E. Oldfield, Structure and cation effects on phosphorus-31 NMR chemical shifts and chemical-shift anisotropies of orthophosphates, *J. Magn. Reson.* 70 (1986) 408–415, [http://dx.doi.org/10.1016/0022-2364\(86\)90129-0](http://dx.doi.org/10.1016/0022-2364(86)90129-0).
- [27] R.K. Brow, C.C. Phifer, G.L. Turner, R.J. Kirkpatrick, Cation effects on ^{31}P MAS NMR chemical shifts of metaphosphate glasses, *J. Am. Ceram. Soc.* 74 (1991) 1287–1290, <http://dx.doi.org/10.1111/jace.1991.74.issue-610.1111/j.1151-2916.1991.tb04099.x>.
- [28] W. Müller-Warmuth, G.W. Schulz, N. Neuroth, F. Meyer, E. Deeg, Protonen in gläsern, *Z. Naturforsch. A* 20a (1965) 902–917, <http://dx.doi.org/10.1515/zna-1965-0706>.
- [29] B.D. Mosel, W. Müller-Warmuth, H. Dutz, The structure of alkali silicate glasses as studied by ^{29}Si NMR absorption and adiabatic fast passage, *Phys. Chem. Glasses* 15 (1974) 154–157.
- [30] S. Sen, J. Stebbins, Phase separation, clustering, and fractal characteristics in glass: a magic-angle-spinning nmr spin-lattice relaxation study, *Phys. Rev. B* 50 (1994) 822–830, <http://dx.doi.org/10.1103/PhysRevB.50.822>.
- [31] S. Sen, Spectroscopic observation of fractal packing of oxygen in variably modified glassy tetrahedral networks, *J. Phys. Chem. Lett.* 5 (2014) 555–559, <http://dx.doi.org/10.1021/jz402730u>.
- [32] R.H. Lamoreaux, D.L. Hildenbrand, High temperature vaporization behavior of oxides. I. Alkali metal binary oxides, *J. Phys. Chem. Ref. Data* 13 (1984) 151, <http://dx.doi.org/10.1063/1.555706>.
- [33] R.H. Lamoreaux, D.L. Hildenbrand, L. Brewer, High-temperature vaporization behavior of oxides II. Oxides of Be, Mg, Ca, Sr, Ba, B, Al, Ga, In, Tl, Si, Ge, Sn, Pb, Zn, Cd, and Hg, *J. Phys. Chem. Ref. Data* 16 (1987) 419, <http://dx.doi.org/10.1063/1.555799>.
- [34] J.F. Stebbins, S. Sen, Oxide ion speciation in potassium silicate glasses: new limits from ^{17}O NMR, *J. Non-Cryst. Solids* 368 (2013) 17–22, <http://dx.doi.org/10.1016/j.jnoncrsol.2013.02.024>.
- [35] M.A. Eastman, P.J. Grandinetti, Y.K. Lee, A. Pines, Double-tuned hopping-coil probe for dynamic-angle spinning NMR, *J. Magn. Reson.* 98 (1992) 333–341.
- [36] J.L. Markley, W.J. Horsley, M.P. Klein, Spin-lattice relaxation measurements in slowly relaxing complex spectra, *J. Chem. Phys.* 55 (1971) 3604–3605, <http://dx.doi.org/10.1063/1.1676626>.
- [37] A. Bax, N.M. Szevenyi, G.E. Maciel, Correlation of isotropic shifts and chemical shift anisotropies by two-dimensional Fourier-transform magic-angle hopping NMR spectroscopy, *J. Magn. Reson.* 52 (1983) 147.
- [38] P.J. Grandinetti, J.H. Baltisberger, A. Llor, Y.K. Lee, U. Werner, M.A. Eastman, A. Pines, Pure absorption-mode lineshapes and sensitivity in two-dimensional dynamic angle spinning NMR, *J. Magn. Reson. A* 103 (1993) 72–81.
- [39] H.Y. Carr, E.M. Purcell, Effects of diffusion on free precession in nuclear magnetic resonance experiments, *Phys. Rev.* 94 (1954) 630–638, <http://dx.doi.org/10.1103/PhysRev.94.630>.
- [40] S. Meiboom, D. Gill, Modified spin-echo method for measuring nuclear relaxation times, *Rev. Sci. Instrum.* 29 (1958) 688.
- [41] K. Dey, J.T. Ash, N.M. Trease, P.J. Grandinetti, Trading sensitivity for information: CPMG acquisition in solids, *J. Chem. Phys.* 133 (2010) 054501-01–054501-10, <http://dx.doi.org/10.1063/1.3463653>.
- [42] R.R. Ernst, G. Bodenhausen, A. Wokaun, Principles of Nuclear Magnetic Resonance in One and Two Dimensions, Oxford University Press, Oxford, 1987.

- [43] R.K. Harris, E.D. Becker, S.M.C. De Menezes, P. Grangerd, R.E. Hoffman, K.W. Zilm, Further conventions for NMR shielding and chemical shifts, IUPAC recommendations 2008, *Solid State Nucl. Mag.* 3 (2008) 41–56, <http://dx.doi.org/10.1016/j.ssnmr.2008.02.004>.
- [44] S. Brooks, A. Gelman, G. Jones, X.-L. Meng (Eds.), *Handbook of Markov Chain Monte Carlo*, Chapman and Hall/CRC Handbooks of Modern Statistical Methods, Chapman and Hall/CRC, Boca Raton, FL, USA, 2011, <http://dx.doi.org/10.1201/CHHANMODSTA10.1201/b10905>.
- [45] D.W. Alderman, M.S. Solum, D.M. Grant, Methods for analyzing spectroscopic line shapes. NMR solid powder patterns, *J. Chem. Phys.* 84 (1986) 3717.
- [46] A. Azzalini, A. Capitanio, *The Skew-Normal and Related Families*, Institute of Mathematical Statistics Monographs, Cambridge University Press, Cambridge, UK, 2014.
- [47] K.P. Balanda, H.L. MacGillivray, Kurtosis: a critical review, *Am. Stat.* 42 (1988) 111, <http://dx.doi.org/10.2307/2684482>.
- [48] G. Czjzek, J. Fink, F. Götz, H. Schmidt, J.M.D. Coey, J.-P. Rebouillat, A. Liénard, Atomic coordination and the distribution of electric field gradients in amorphous solids, *Phys. Rev. B* 23 (1981) 2513–2530, <http://dx.doi.org/10.1103/PhysRevB.23.2513>.
- [49] G.L. Caër, R.A. Brand, General models for the distributions of electric field gradients in disordered solids, *J. Phys.: Condens. Matter* 10 (1998) 10715–10774, <http://dx.doi.org/10.1088/0953-8984/10/47/020>.
- [50] J.-B. d'Espinose de Lacaillerie, C. Fretigny, D. Massiot, MAS NMR spectra of quadrupolar nuclei in disordered solids: the Czjzek model, *J. Magn. Reson.* 192 (2008) 244–251, <http://dx.doi.org/10.1016/j.jmr.2008.03.001>.
- [51] G.L. Caër, B. Bureau, D. Massiot, An extension of the Czjzek model for the distributions of electric field gradients in disordered solids and an application to NMR spectra of ^{71}Ga in chalcogenide glasses, *J. Phys.: Condens. Matter* 22, doi: <http://dx.doi.org/10.1088/0953-8984/22/6/065402>.
- [52] F. Vasconcelos, S. Cristol, J.-F. Paul, L. Delevoye, F. Mauri, T. Charpentier, G.L. Caër, Extended czjzek model applied to NMR parameter distributions in sodium metaphosphate glass, *J. Phys.: Condens. Matter* 25, doi: <http://dx.doi.org/10.1088/0953-8984/25/25/255402>.
- [53] M.J. Frisch, G.W. Trucks, H.B. Schlegel, G.E. Scuseria, M.A. Robb, J.R. Cheeseman, J.A. Montgomery, T. Vreven, K.N. Kudin, J.C. Burant, J.M. Millam, S.S. Iyengar, J. Tomasi, V. Barone, B. Mennucci, M. Cossi, G. Scalmani, N. Rega, G.A. Petersson, H. Nakatsuji, M. Hada, M. Ehara, K. Toyota, R. Fukuda, J. Hasegawa, M. Ishida, T. Nakajima, Y. Honda, O. Kitao, H. Nakai, M. Klene, X. Li, J.E. Knox, H.P. Hratchian, J.B. Cross, V. Bakken, C. Adamo, J. Jaramillo, R. Gomperts, R.E. Stratmann, O. Yazyev, A.J. Austin, R. Cammi, C. Pomelli, J.W. Ochterski, P.Y. Ayala, K. Morokuma, G.A. Voth, P. Salvador, J.J. Dannenberg, V.G. Zakrzewski, S. Dapprich, A.D. Daniels, M.C. Strain, O. Farkas, D.K. Malick, A.D. Rabuck, K. Raghavachari, J.B. Foresman, J.V. Ortiz, Q. Cui, A.G. Baboul, S. Clifford, J. Cioslowski, B.B. Stefanov, G. Liu, A. Liashenko, P. Piskorz, I. Komaromi, R.L. Martin, D.J. Fox, T. Keith, M.A. Al-Laham, C.Y. Peng, A. Nanayakkara, M. Challacombe, P.M.W. Gill, B. Johnson, W. Chen, M.W. Wong, C. Gonzalez, J.A. Pople, *Gaussian 03*, 2003.
- [54] L. Le Page, L.D. Calvert, E.J. Gabe, Parameter variation in low-quartz between 94 and 298 K, *J. Phys. Chem. Solids* 41 (1980) 721–725.
- [55] W. Blumberg, Nuclear spin-lattice relaxation caused by paramagnetic impurities, *Phys. Rev.* 119 (1960) 79–84, <http://dx.doi.org/10.1103/PhysRev.119.79>.
- [56] I. Lowe, D. Tse, Nuclear spin-lattice relaxation via paramagnetic centers, *Phys. Rev.* 166 (1968) 279–291, <http://dx.doi.org/10.1103/PhysRev.166.279>.
- [57] D. Tse, S. Hartmann, Nuclear spin-lattice relaxation via paramagnetic centers without spin diffusion, *Phys. Rev. Lett.* 21 (1968) 511–514, <http://dx.doi.org/10.1103/PhysRevLett.21.511>.
- [58] J. Bodart, V. Bork, T. Cull, H. Ma, P. Fedders, D. Leopold, R. Norberg, Recovery of nuclear magnetization under extreme inhomogeneous broadening, *Phys. Rev. B* 54 (1996) 15291–15298, <http://dx.doi.org/10.1103/PhysRevB.54.15291>.
- [59] C. Nelson, W.B. White, Transition metal ions in silicate melts—I. Manganese in sodium silicate melts, *Geochim. Cosmochim. Acta* 44 (1980) 887–893, [http://dx.doi.org/10.1016/0016-7037\(80\)90269-0](http://dx.doi.org/10.1016/0016-7037(80)90269-0).
- [60] C. Nelson, T. Furukawa, W.B. White, Transition metal ions in glasses: network modifiers or quasi-molecular complexes?, *Mater. Res. Bull.* 18 (1983) 959–966, [http://dx.doi.org/10.1016/0025-5408\(83\)90007-7](http://dx.doi.org/10.1016/0025-5408(83)90007-7).
- [61] C. Nelson, W.B. White, Transition metal ions in silicate melts. IV. Cobalt in sodium silicate and related glasses, *J. Mater. Res.* 1 (1986) 130–138, <http://dx.doi.org/10.1557/JMR.1986.0130>.
- [62] H. Keppler, Crystal field spectra and geochemistry of transition metals in silicate melts and glasses, *Am. Miner.* 77 (1992) 62–75.
- [63] B.O. Mysen, P. Richet, *Silicate Glasses and Melts, Properties and Structure*, Elsevier, 2005.
- [64] J.V. Smith, C.S. Blackwell, Nuclear magnetic resonance of silica polymorphs, *Nature* 303 (1983) 223–225, <http://dx.doi.org/10.1038/303223a0>.
- [65] F. Mauri, A. Pasquarello, B.G. Pfommer, Y.-G. Yoon, S.G. Louie, Si–O–Si bond-angle distribution in vitreous silica from first-principles, *Phys. Rev. B* 62 (2000) R4786–R4789, <http://dx.doi.org/10.1103/PhysRevB.62.R4786>.
- [66] R. Witter, P. Hartmann, J. Vogel, C. Jäger, Measurements of chain length distribution in chain phosphate glasses using 2D ^{31}P double quantum NMR, *Solid State NMR* 13 (1998) 189–200.
- [67] L. Olivier, X. Yuan, A.N. Cormack, C. Jäger, Combined ^{29}Si double quantum NMR and MD simulation studies of network connectivities of binary $\text{Na}_2\text{O} \cdot \text{SiO}_2$ glasses: new prospects and problems, *J. Non-Cryst. Solids* 293–295 (2001) 53–66.
- [68] L. Martel, D. Massiot, M. Deschamps, Phase separation in sodium silicates observed by solid-state MAS-NMR, *J. Non-Cryst. Solids* 390 (2014) 37–44, <http://dx.doi.org/10.1016/j.jnoncrsol.2014.02.015>.
- [69] A. Navrotsky, *Energetics of Silicate Melts, Reviews in Mineralogy*, vol. 32, Mineralogical Society of America, Washington, DC, 1995, pp. 121–143.
- [70] P.C. Hess, Thermodynamic Mixing Properties and the Structure of Silicate Melts, *Reviews in Mineralogy*, vol. 32, Mineralogical Society of America, Washington, DC, 1995, pp. 145–190.
- [71] W.H. Zachariasen, The atomic structure in glass, *J. Am. Chem. Soc.* 54 (1932) 3841–3851.
- [72] E.D. Lacy, A statistical model of polymerisation/depolymerisation relationship in silicate melts and glasses, *Phys. Chem. Glasses* 6 (5) (1965) 171–180.
- [73] A.-R. Grimmer, ^{31}P NMR and π bond in solid phosphorus compounds, *Spectrochim. Acta A: Molec. Spect.* 34 (1978) 941, [http://dx.doi.org/10.1016/0584-8539\(78\)80015-4](http://dx.doi.org/10.1016/0584-8539(78)80015-4).
- [74] R. Brow, R. Kirkpatrick, G. Turner, The short range structure of sodium phosphate glasses I. MAS NMR studies, *J. Non-Cryst. Solids* 116 (1990) 39–45, [http://dx.doi.org/10.1016/0022-3093\(90\)91043-Q](http://dx.doi.org/10.1016/0022-3093(90)91043-Q).
- [75] R. Kirkpatrick, R.K. Brow, Nuclear magnetic resonance investigation of the structures of phosphate and phosphate-containing glasses: a review, *Solid State NMR* 5 (1995) 9–21, [http://dx.doi.org/10.1016/0926-2040\(95\)00042-O](http://dx.doi.org/10.1016/0926-2040(95)00042-O).
- [76] G. Engelhardt, D. Michel, *High-resolution Solid-state NMR of Silicates and Zeolites*, John Wiley & Sons, Chichester, 1987.
- [77] V. Schomaker, D.P. Stevenson, Some revisions of the covalent radii and the additivity rule for the lengths of partially ionic single covalent bonds, *J. Am. Chem. Soc.* 63 (1941) 37–40, <http://dx.doi.org/10.1021/ja01846a007>.
- [78] L. Pauling, *The Nature of the Chemical Bond*, Cornell University Press, Ithaca, NY, 1960.
- [79] W. Gordy, A new method of determining electronegativity from other atomic properties, *Phys. Rev. B* 69 (1946) 604–607, <http://dx.doi.org/10.1103/PhysRev.69.604>.
- [80] R.P. Iczkowski, J.L. Margrave, Electronegativity, *J. Am. Chem. Soc.* 83 (1961) 3547–3551, <http://dx.doi.org/10.1021/ja01478a001>.
- [81] J.E. Huheey, *Inorganic Chemistry*, Harper and Row, 1983.
- [82] E.J.W. Whittaker, R. Muntus, Ionic radii for use in geochemistry, *Geochim. Cosmochim. Acta* 34 (1970) 945–956, [http://dx.doi.org/10.1016/0016-7037\(70\)90077-3](http://dx.doi.org/10.1016/0016-7037(70)90077-3).
- [83] P.J. Grandinetti, J.H. Baltisberger, U. Werner, A. Pines, I. Farnan, J.F. Stebbins, Solid-state ^{17}O magic-angle and dynamic-angle spinning NMR study of coesite, *J. Phys. Chem.* 99 (1995) 12341–12348.
- [84] T.M. Clark, P.J. Grandinetti, P. Florian, J.F. Stebbins, An ^{17}O NMR investigation of crystalline sodium metasilicate: Implications for the determinations of local structure in alkali silicates, *J. Phys. Chem. B* 105 (2001) 12257–12265.
- [85] T.M. Clark, P.J. Grandinetti, Dependence of bridging oxygen O– ^{17}O quadrupolar coupling parameters on Si–O distance and Si–O–Si angle, *J. Phys. Condens. Matter* 15 (2003) S2387–S2395.
- [86] T.M. Clark, P.J. Grandinetti, Calculation of bridging oxygen ^{17}O quadrupolar coupling parameters in alkali silicates: a combined ab initio investigation, *Solid State NMR* 27 (2005) 233–241, <http://dx.doi.org/10.1016/j.ssnmr.2005.01.002>.
- [87] P.J. Grandinetti, T.M. Clark, *The Structure of Oxide Glasses: Insights from ^{17}O NMR*, Springer, Netherlands, 2006, http://dx.doi.org/10.1007/1-4020-3910-7_174, pp. 1563–1568.
- [88] C. Bonhomme, C. Gervais, F. Babonneau, C. Coelho, F. Pourpoint, T. Azais, S.E. Ashbrook, J.M. Griffin, J.R. Yates, F. Mauri, C.J. Pickard, First-principles calculation of nmr parameters using the gauge including projector augmented wave method: a chemist's point of view, *Chem. Rev.* 112 (2012) 5733–5779, <http://dx.doi.org/10.1021/cr300108a>.
- [89] H.K.C. Timken, S.E. Schramm, R.J. Kirkpatrick, E. Oldfield, Solid-state oxygen- 17 nuclear magnetic resonance spectroscopic studies of alkaline earth metasilicates, *J. Phys. Chem.* 91 (1987) 1054–1058.
- [90] T.M. Clark, P.J. Grandinetti, Factors influencing the ^{17}O quadrupole coupling constant in bridging oxygen environments, *Solid State NMR* 16 (2000) 55–62.
- [91] U. Hoppe, A structural model for phosphate glasses, *J. Non-Cryst. Solids* 195 (1996) 138–147, [http://dx.doi.org/10.1016/0022-3093\(95\)00524-2](http://dx.doi.org/10.1016/0022-3093(95)00524-2).
- [92] G.N. Greaves, EXAFS and the structure of glass, *J. Non-Cryst. Solids* 71 (1985) 203–217.
- [93] B. Vessal, G.N. Greaves, P.T. Marten, A.V. Chadwick, R. Mole, S. Houde-Walter, Cation microsegregation and ionic mobility in mixed alkali glasses, *Nature* 356 (1992) 504–506.
- [94] A. Pedone, G. Malavasi, M.C. Menziani, A.N. Cormack, U. Segre, A new self-consistent empirical interatomic potential model for oxides, silicates, and silica-based glasses, *J. Phys. Chem. B* 110 (2006) 11780–11795, <http://dx.doi.org/10.1021/jp0611018>.
- [95] A. Pedone, G. Malavasi, A.N. Cormack, U. Segre, M.C. Menziani, Insight into elastic properties of binary alkali silicate glasses; prediction and interpretation through atomistic simulation techniques, *Chem. Mater.* 19 (2007) 3144–3154, <http://dx.doi.org/10.1021/cm062619r>.
- [96] J.C. Mauro, C.S. Philip, D.J. Vaughn, M.S. Pambianchi, Glass science in the united states: current status and future directions, *Intl. J. Appl. Glass Sci.* 5 (2014) 2–15, <http://dx.doi.org/10.1111/ijag.2014.5.issue-110.1111/ijag.12058>.
- [97] J. Phillips, Topology of covalent non-crystalline solids I: short-range order in chalcogenide alloys, *J. Non-Cryst. Solids* 34 (1979) 153–181, [http://dx.doi.org/10.1016/0022-3093\(79\)90033-4](http://dx.doi.org/10.1016/0022-3093(79)90033-4).

- [98] J. Phillips, M. Thorpe, Constraint theory, vector percolation and glass formation, *Solid State Commun.* 53 (1985) 699–702, [http://dx.doi.org/10.1016/0038-1098\(85\)90381-3](http://dx.doi.org/10.1016/0038-1098(85)90381-3).
- [99] M. Thorpe, Continuous deformations in random networks, *J. Non-Cryst. Solids* 57 (1983) 355–370, [http://dx.doi.org/10.1016/0022-3093\(83\)90424-6](http://dx.doi.org/10.1016/0022-3093(83)90424-6).
- [100] H. He, M. Thorpe, Elastic properties of glasses, *Phys. Rev. Lett.* 54 (1985) 2107–2110, <http://dx.doi.org/10.1103/PhysRevLett.54.2107>.
- [101] Y. Cai, M. Thorpe, Floppy modes in network glasses, *Phys. Rev. B* 40 (1989) 10535–10542, <http://dx.doi.org/10.1103/PhysRevB.40.10535>.
- [102] P.K. Gupta, J.C. Mauro, Composition dependence of glass transition temperature and fragility. i. A topological model incorporating temperature-dependent constraints, *J. Chem. Phys.* 130 (2009) 094503, <http://dx.doi.org/10.1063/1.3077168>.
- [103] J.C. Mauro, P.K. Gupta, R.J. Loucks, Composition dependence of glass transition temperature and fragility. II. A topological model of alkali borate liquids, *J. Chem. Phys.* 130 (2009) 234503, <http://dx.doi.org/10.1063/1.3152432>.
- [104] J.C. Phillips, R. Kerner, Structure and function of window glass and pyrex, *J. Chem. Phys.* 128 (2008) 174506, <http://dx.doi.org/10.1063/1.2805043>.
- [105] M.M. Smedskjaer, J.C. Mauro, S. Sen, Y. Yue, Quantitative design of glassy materials using temperature-dependent constraint theory, *Chem. Mater.* 22 (2010) 5358–5365, <http://dx.doi.org/10.1021/cm1016799>.
- [106] M.M. Smedskjaer, J.C. Mauro, S. Sen, J. Deubener, Y. Yue, Impact of network topology on cationic diffusion and hardness of borate glass surfaces, *J. Chem. Phys.* 133 (2010) 154509, <http://dx.doi.org/10.1063/1.3497036>.
- [107] M.M. Smedskjaer, J.C. Mauro, R.E. Youngman, C.L. Hogue, M. Potuzak, Y. Yue, Topological principles of borosilicate glass chemistry, *J. Phys. Chem. B* 115 (2011) 12930–12946, <http://dx.doi.org/10.1021/jp208796b>.